GPPS-NA-2018-128

ON CLEAN INFLOW TESTING
FOR INTERMEDIATE TURBINE DUCTS

M. Steiner
Graz University of Technology
michael.steiner@tugraz.at
Graz, Austria

A. Peters
GE Aviation
andreas.peters@ge.com
Munich, Germany

G. Gatti
Politecnico di Milano
giacomo.gatti@polimi.it
Milano, Italy

C. Zscherp, K. Engel
MTU Aero Engines
karl.engel@mtu.de
Munich, Germany

**I. Cabona, A. Ramesh, P.Z.
Sterzinger, F. Heitmeir, E. Göttlich**
Graz University of Technology
emil.goettlich@tugraz.at
Graz, Austria

ABSTRACT

In this paper, an investigation on the effect of different inlet conditions on an engine representative turbine centre frame (TCF) is presented. A comparison between three cases is obtained in the new high speed annular cascade rig at the Institute for Thermal Turbomachinery and Machine Dynamics at Graz University of Technology. Differing from the engine realistic inlet conditions, a case with clean inflow, a case with IGVs and a case with IGVs and with spoke wheel are considered. Furthermore, a fourth inlet case is taken into account, namely the case with the unshrouded, uncooled HPT imposed inlet flow condition (rotating rig).

A back-to-back comparison of the inlet and exit flow fields is based on time averaged data, obtained by five-hole-probe measurements. For the flow through the duct, the pressure rise coefficient at the duct hub and case as well as along the strut surface is evaluated. In addition, a state-of-the-art oil flow visualisation technique is used to determine the change of the wall shear stresses in the duct. CFD simulations also support the discussion and give additional insight into the flow behaviour.

The major outcomes of the present study are that the investigated duct, not separating downstream of the HPT stage, does separate when unsteady effects are removed. Moreover, the duct efficiency cannot be foreseen from clean inflow testing, since the throughflow is completely different. Finally, radial exit profiles can be matched along all four cases presented, with reasonable agreement.

INTRODUCTION

Since 2005 a series of different configurations of intermediate turbine ducts (ITDs) have been tested in the transonic test turbine facility at the Institute for Thermal Turbomachinery and Machine Dynamics at Graz University of Technology. In order to gain a new insight into flow physics and loss generation mechanisms, TCFs with turning vanes or straight strut fairings were investigated at engine-representative operating conditions. In addition, absolute performance levels were pursued. Aside the experimental results also steady RANS CFD showed a significant change of the duct aerodynamics and duct secondary flows related to the high-pressure turbine (HPT) exit flow field. Anyway, the performances of TCFs were over-estimated with respect to the results of the experimental analysis and not even unsteady RANS simulations have fulfilled this gap.

To shed light on the differences between CFD and measurements a new facility with an ideal clean inflow was designed and commissioned. A spoke wheel was also designed to generate distinct rotating wakes, which should simulate the unsteady wake effects of the HPT. The new annular cascade test bench and the pre-existing transonic test turbine facility can accommodate the same components, which combined with their measurement techniques, enable back-to-back testing.

Usually, the duct is selected to be conservative, namely to operate far away from a possible flow separation at the casing. Although it is well established that the performance of a TCF is significantly influenced by the upstream HPT as well as the downstream LPT (Göttlich, 2011), a common way to prove this criterion, is to perform clean inflow testing. Following the different steps from the literature, this contribution selects as a first case of study, a clean inflow test, which gives similar results to those gained by Dominy & Kirkham (1995). Further they stated, the effect of the inlet swirl is favourable to the
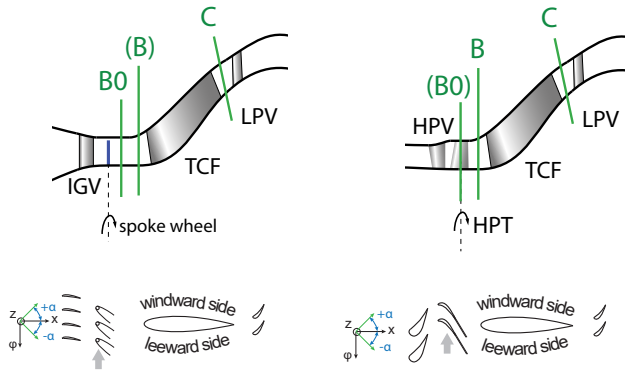
Figure 1: Experimental Setup in AnCa and TTTF - section and blade to blade view

radial pressure gradient, the wakes energise the boundary layer and increase the turbulence level (Dominy & Kirkham, 1996). Therefore, this study investigated a second case with inlet guide vanes as well as a third case with a spoke wheel, adding periodically incoming wakes. This spoke wheel is not only adding the wakes, but it also generates a tip jet and some vortical structures similar to a tip leakage vortex. As investigated by Göttlich, et al. (2007), Marn, et al. (2007), Sanz, et al. (2009) and Mimic et al. (2017) the tip gap and the tip leakage vortex give a positive contribution to the low energy fluid at the duct casing.

To the authors' knowledge, no literature compares an engine representative TCF in a back-to-back comparison, as done in this paper. The main advantage of the present analysis is the possibility to find a direct relationship between the overall efficiency and the inlet condition, not depending on the shape of the duct itself.

Facility

Two facilities are addressed in this work, both driven by pressurised air delivered by a 3 MW compressor station. One is a newly built high-speed annular cascade test bench (AnCa); the other is the existing transonic test turbine facility (TTTF). While the AnCa is providing a clean inflow, where IGVs and a spoke wheel can be placed, the TTTF includes an uncooled, unshrouded, fully purged single stage HPT (aerodynamically representative of a second-stage HPT engine definition) upstream of the component of interest, the TCF. The interested reader can find more details on the TTTF setup used in this work in Steiner, et al. (2017). The AnCa is designed to accommodate test hardware identical to the TTTF (TCF, LPV, Deswirler) which, combined with consistent measurement techniques, enables direct back-to-back testing. Both facilities provide engine-representative conditions at the TCF inlet (TCF inlet Mach number, inlet swirl, Reynolds numbers (based on TCF axial chord) of one million and higher, strouhal number and HPT corrected speed). The Aero Design Point (ADP) for the HPT case was selected with a mass flow rate of 13.3 kg/s, a rig inlet to outlet pressure ratio of 2.81 and a HPT rotor speed of 9570 rpm. The spoke wheel could not be selected matching the similarity parameters based on LP blade-wake interactions as suggested by, for example Schulte & Hodson (1998). The limits of the electric motor restricted
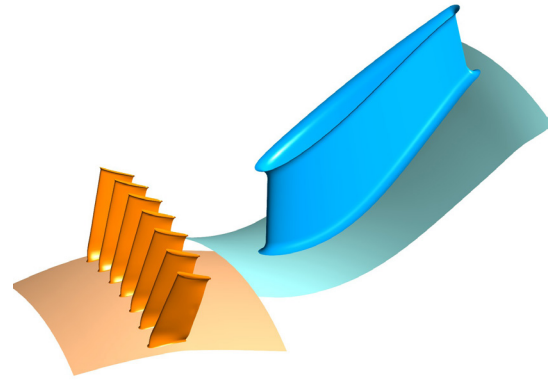
Figure 2: Numerical Setup of the case w/ IGVs

the rod diameter at 75% of the HP blade thickness, the flow coefficient to be over 6 times higher and the reduced frequency to be 15% of the HPT case. Only the tip gap to blade (rod) height ratio was within a comparable range of 0.4%.

Measurement Technique

The measurement system was kept the same for both test facilities. It consists of several PSI 9016 multi-pressure scanner modules and a NI cRIO-9067 controller equipped with NI 9214 temperature measurement modules as well as current analogue input modules. In total, over 465 values are read simultaneously with a sampling frequency of 5 [Hz]. For the investigations in the current work, three critical measurement techniques are described in more detail.

First, two five-hole probes with a head diameter of 2.5mm (manufactured and calibrated by IST, RWTH Aachen) are used for traverse measurements at the TCF inlet and exit planes. Figure 1 gives a schematic cross section of the two facilities, highlighting the corresponding planes B0, B and C, respectively. For measurements performed in the AnCa, the TCF inlet plane B0 was used. In the TTTF, the limited space between the HPT and TCF struts resulted in the need for a stationary plane B. In this case, the probe was circumferentially fixed in-between two struts and the HPT stator was traversed along 3.3 vanes. A comparison between this so-called pseudo traverse and the actual traverse downstream of an HPT rotor is given by Faustmann & Göttlich (2014) and shows very close agreement. The TCF exit plane C was identical for both setups, with an inclined measurement plane and five-hole probe head, to ensure alignment of the probe head with the mean flow angle. In circumferential and radial direction, the probe was traversed to pre-defined locations. While those related to the circumferential direction were equally spaced, the radial points were sparse at midspan and refined close to the end - walls. To reduce the measurement uncertainty and ensure a measurement within the calibration, the probe was turned into the flow for each measurement point. Table 1 summarises the mean uncertainties including the systematic error of the PSI Module of ±100 [Pa] and the uncertainty in the multi-parameter approximation. Additional uncertainties may arise when measuring the time-mean conditions downstream of rotating wakes (Bauinger, et al., 2017).

Second, an oil flow visualization technique was used to identify the wall shear stress trajectories in the TCF passage.

$$\frac{DP}{P} = \frac{\bar{p}_{t,Inlet} - \bar{p}_{t,Exit}}{\bar{p}_{t,Exit}} \qquad (1)$$

$$c_p = \frac{p_s - \bar{p}_{s,Inlet}}{\bar{p}_{t,Inlet} - \bar{p}_{s,Inlet}} \qquad (2)$$

A mixture of titanium oxide (TiO2) and synthetic motor oil was applied in the passage. To better identify flow migration, the viscous mixture was coloured white for the strut end-walls and red for the hub and the casing. The operating point was kept constant for a given period, to allow for a representative picture after the rig was shut down.

Third, the pressure coefficient along the casing and hub end-wall was measured with ten and thirteen wall flush taps (diameter of 0.6mm), placed at mid-pitch in-between two struts, respectively. Connected to a PSI 9016 module, the measurement accuracy is within ±100 [Pa].

Data Reduction

The five-hole probe data was post-processed to generate contour plots and circumferentially mass-averaged radial profiles. For the AnCa case, the radial lines are averaged across 7 IGV pitches, while in the TTTF case 3 HP vanes were considered. At the TCF exit, the flow was averaged over one TCF strut pitch. All data is normalised by the corresponding mass-averaged value (in circumferential and radial direction) of the reference case clean inflow. For all four cases, the pressure loss was derived from the mass-averaged single value according to equation 1.

The oil flow visualisation data was post-processed using picture editing tools, to enhance the contrast of the colours and to trace some trajectories. The static pressure is presented as a non-dimensional coefficient according to equation 2.

Numerical Setup

For a qualitative assessment of the flow behaviour, two numerical investigations of the AnCa were performed. One for a case with IGVs and one for a case with IGVs and spoke wheel. The commercial code ANSYS CFX 16.2 was used for all the computations presented in this paper. Since the aim was to leverage the numerical results to interpret the flow characteristics, URANS simulations with matching periodicity (7 IGVs, 1 TCF passage including one strut, no pitch-wise scaling) were set up. This allows the use of direct interfaces and thus a modelling of possible wake instability effects. The k-ω SST model was chosen for turbulence closure; thus, the grid spacing near the walls was set to ensure a y^+ value lower than 1. Furthermore, additional radial refinement was introduced in the first 5% of the channel height both at the hub and at the tip, to accurately model the fillets. This leads to a total mesh size of approximately 9 million cells. Figure 2 shows an overview of the computational domain.

Radial profiles of total pressure and flow angle were imposed as inlet boundary condition, as well as a section-average value of total temperature. At the outlet, a section-average distribution of static pressure was set. The time step (Delta t = 5·10⁻⁶ s) was chosen to resolve at least three harmonics of the theoretical vortex shedding frequency of the IGVs and to guarantee that the solution does not depend on

Table 1: Measurement uncertainty and calibration range for the two used five-hole probes

Flow Quantity	Unit	Uncertainty		Calibration Range
Mach Number (Ma)	[-]	0.005	-0.004	0.1 to 0.8
Yaw Angle (α)	[deg]	0.3	-0.3	-20 to 20
Pitch Angle (γ)	[deg]	0.5	-0.4	-20 to 20
Total pressure (pt)	[Pa]	300	-300	-
Total Temperature(Tt)	[K]	0.6	-0.5	-

it. For the case with spoke wheel, the same time step resolves more than 1/50 of the rods blade passing frequency.

Operating Conditions

Determining a comparable operating point for these four cases proved to be challenging. Usually, a combination of corrected mass flow, corrected speed and pressure ratio is set to ensure similarity of the turbine inlet and exit velocity triangles under small changes of thermodynamic conditions. However, in the AnCa tests, the inlet section area and flow angles were changed. To compare the four cases, a decision was made to hold the absolute level of Mach number at the TCF inlet constant. For this purpose, the Mach number at 50% channel height was compared by means of five-hole probe measurements. For Reynolds number similarity, and to enable loss comparisons, the total temperature at the TCF inlet was also held constant.

RESULTS AND DISCUSSION

TCF Inflow

Radial profiles at the TCF inlet (based on circumferentially mass-averaged five-hole probe data) are presented in Fig. 3 in order to compare inflow conditions. The target to achieve a similar Mach number at 50 % channel height for all cases measured in the annular cascade was reached. For the case with the HPT, the mean Mach number at 50% channel height matches the AnCa cases, with a difference of ~10%.

In terms of radial total pressure, the clean inflow case and the case with IGVs match within the measurement uncertainty. The unsteady case with spoke wheel shows a gradient close to the tip as well as a small gradient below the 50% span. Important for ducts is the local inflow gradient of total pressure and Mach number in the tip region (see Sanz et al. (2009)). For the spoke wheel case this is caused by the tip jet and a pair of trailing vortices (or tip vortices) emerging from the free end of the rods (more in (Sumner, 2013)). For the HPT case, this is caused by the tip leakage vortex which can be found at 87% span and the upper passage vortex from the rotor at 80% span. Further impact of the secondary effects of the HPT can be found close to the hub. There the lower passage vortex of the rotor and the stator impact at 15% and 6% span, respectively. For an interested reader a detailed discussion on the flow exiting the same HPT can be found in Zerobin et al. (2017). Although the effects are different, the comparison between the spoke wheel and the HPT case show a similar gradient in total pressure above 87% span. The Mach number is reduced for the HPT case at midspan, but it shows a reasonable agreement
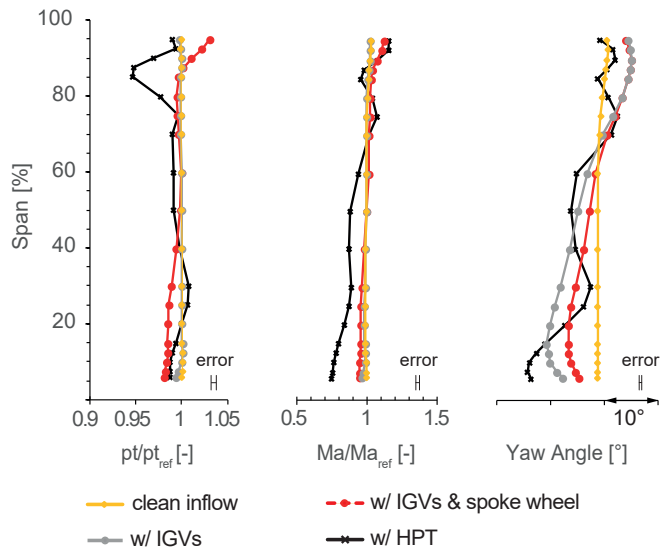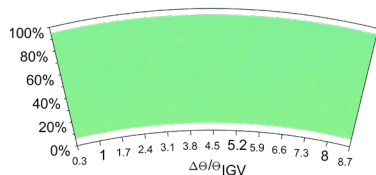
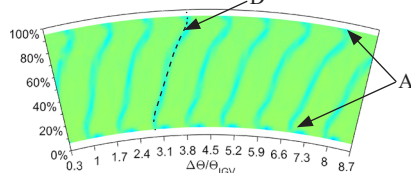**Figure 3: Radial TCF Inlet Profiles (Plane B/B0)**

for the upper 10% span.

    In the case of the yaw angle (in Fig. 3), the clean inflow shows a vertical radial distribution, with an unavoidable slight offset to a straight axial flow. The IGVs then change the yaw angle and the radial gradient, close to the case with an HPT. Adding the spoke wheel changes the yaw angle across the channel height again, while above 80% the flow angle stays
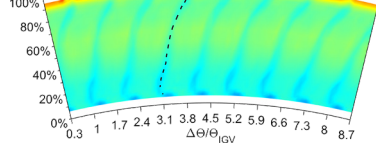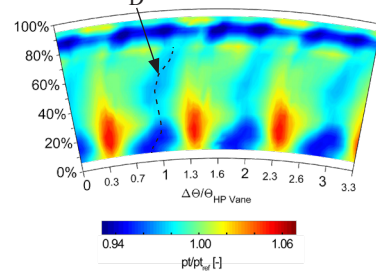
Figure 5: Radial TCF Exit Profiles (Plane C)
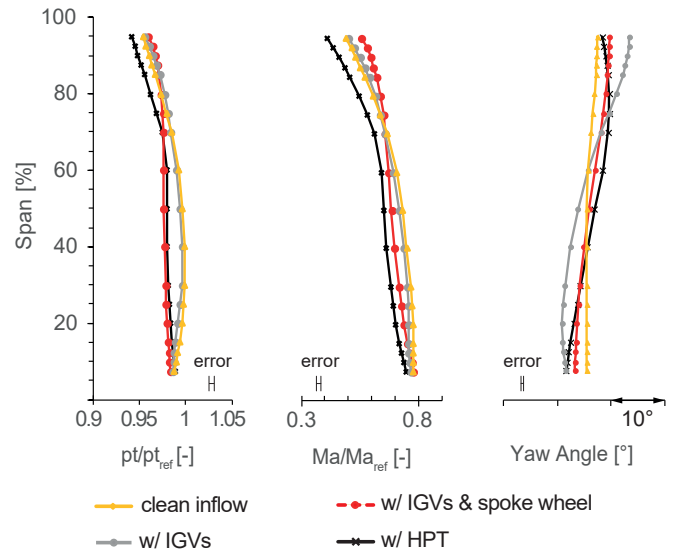
identical. First, the added blockage of the rods raises the axial flow velocity and changes the yaw angle more towards axial flow. Second, the rotational speed changes the absolute velocity vector in the wake flow and tilt the radial profile. As the pitch of the bars is changing in radial direction, the effect is 4% higher at the hub.

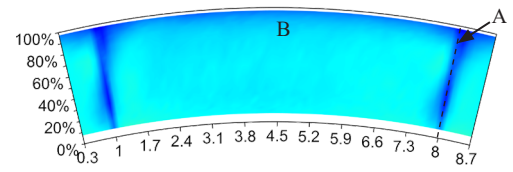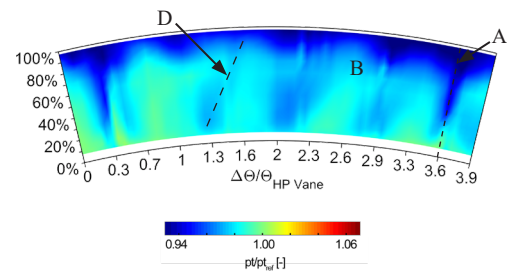   Figure 4 shows the total pressure contours at the duct inlet

Figure 4: Total pressure contours for the different cases at the inlet of the TCF (view is A.L.F.)
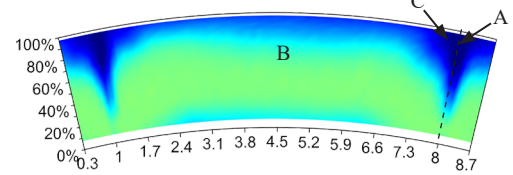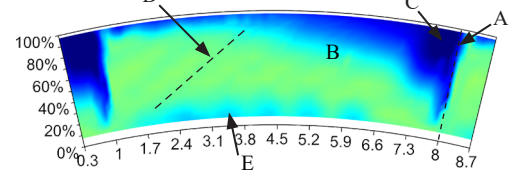
Figure 6: Total pressure contours for the different cases at the exit of the TCF (view is A.L.F.)

for all four cases in the view A.L.F.. The first case, with clean inflow (Fig. 4.1), shows no circumferential variations, while in the second case with IGVs (Fig. 4.2) a periodic pattern of eight thin wakes in the measurement window is visible. The shape of the wake in the tip and hub regions (Fig. 4.2 A) can be linked to two effects. Once the mechanical blade design at the trailing edge and second the secondary flow structures, which stay close to the end - wall, for the given IGV aspect ratio greater than 3. When adding the spoke wheel for the third case, the radial gradient of total pressure, as already visible in the radial distribution, is evident in the field (Fig. 4.3). The IGV wakes are still showing a low total pressure region (Fig. 4.3 D), while the periodically incoming wakes of the rods can be captured by their impact (especially in the tip region), but of course not in an unsteady way. The fourth case is showing the inflow of the TCF downstream of the HPT stage (Fig. 4.4). The contour plot shows a sector covering mechanically 3.3 HP vanes. Their impact on the flow can be seen as a low total pressure region in Fig. 4.4 D. In the measurement plane B (which is 240% axial chord of the vane downstream) not only the chopped and decayed vane wake itself, but also the secondary flows and the low momentum purge flows are responsible for the low energy fluid visible. Furthermore, the tip leakage vortex and the counter-rotating upper passage vortex of the rotor appears as a superimposed low total pressure region at 85% channel height (Fig. 4.4 B).

TCF Exit Flow

Figure 5 shows the circumferentially mass-averaged total pressure, Mach number and yaw angle profiles at the duct exit plane C. The case with the HPT and the case with the spoke wheel can be seen to match within the measurement uncertainty in terms of total pressure in the lower 60% of the channel. Further in the lower 60% of the channel, their Mach number profiles are parallel. Just derived from the radial profiles, it seems that the offset for the HPT case is due to the lower mean inlet Mach number. In terms of a yaw angle comparison for the two mentioned cases, the passage reduces the strong variation for the HPT case and brings them overlay reasonable.

It is worth noting that for all four cases the gradient of total pressure matches in the upper 25% of the channel. Further, the gradients of the Mach number agree as well, except for the case with the spoke wheel. This observation indicates that apart from different local effects at the inflow and different aerodynamic behaviours in the duct, the radial exit profiles of total pressure and Mach number are in terms of their gradient not that sensitive. Since local flow effects contribute to the radial distributions in the TCF exit plane C, the analysis of the complete field (shown in Fig. 6) is carried out.

Figure 6.1 shows the total pressure contour of the first case with clean inflow. The loss cores in the exit flow field are related to the TCF strut wakes (Fig. 6.1 A), the end-wall shear layer (Fig. 6.1 B) and two end-wall vortices (Fig. 6.1 C), one on each side of the strut. The oil flow visualization on the strut surface presented later in this paper will give more insight on the formation of the strut exit flow behaviour. Anyway, it is interesting to note that the strong losses related to the

wake flow of the strut (Fig. 6.1 A) are only present from 40% channel height upwards. Below, the cross passage flow caused by the radial pressure gradient energises the low momentum fluid at the corner of the strut and the hub end-wall. At mid-pitch of the two struts, the thickness of the boundary layer increases (Fig. 6.1 B). This is in line with the findings from Dominy & Kirkham (1996), who observed a similar behaviour in a non-strutted duct with wakes at the inflow. In their case, the cross-passage pressure gradient triggered a radial fluid migration across the wakes. In the tip region, the fluid migration formed vortical structures, which energised and therefore thinned the boundary layer. Göttlich (2011) provides a more detailed sketch for this behaviour. Linked to the current case, the vortical structures energising the boundary layer are associated more with the end-wall and hub cross passage flow (see Fig. 9), than with radial fluid migration.

In the second case, the IGVs are added, resulting in a mean TCF inlet swirl distribution comparable to the case with the actual HPT. Figure 6.2 shows the corresponding exit flow, where the thin inlet wakes induced by the IGVs decayed but are still visible (Fig. 6.2 D). The inlet swirl enhances the wakes to skew and partially merge. Moreover, it seems that the skewed wakes interact with the boundary layer all along the circumference (Fig. 6.2 B), modifying the flow field compared to the clean inflow. The high loss fluid accumulates at the casing, forming a strong loss core close to the strut end-wall (Fig. 6.2 C). This behaviour again confirms earlier findings for generic ducts (Dominy & Kirkham, 1995). Due to the inlet swirl, the wakes are skewed. Their vortices (generated by the cross-passage pressure gradient and the resulting secondary flow structures) with the same sense of rotation merge and locally thicken the boundary layer at the casing. In comparison to the clean inflow, the increased size of the concentrated loss core (Fig. 6.2 C) can be derived from first: the additional losses generated by the wakes, partially transported into the casing boundary layer due to the radial fluid migration, and second, the interaction of this secondary flow, forming small vortices with the casing boundary layer. The position of the concentrated loss core (Fig. 6.2 C) is due to the swirl accumulating the losses on one side of the strut. The loss core related to the strut (Fig. 6.2 A) also increased in comparison to the clean inflow and is now present upwards of 20% channel height. Interesting to note is that due to the swirl in the channel, the loss core only appears at the rotor wake leeward side of the strut.

The exit flow of the third case highlights the additional influence of the spoke wheel. The strong loss cores (Fig. 6.2 A, C) from the case with IGVs are no longer observable, while the strut wake flow (Fig. 6.3 A) is now present along the entire channel height. The strut wake flow is narrowed, showing a comparable small widening in circumferential direction in the tip corner. The IGV wakes, still visible in the inlet section (Fig. 4.3 D), cannot be recognised in the time-averaged exit flow field anymore. That concludes that the IGV wakes completely mix out in the duct flow and fully contribute to the losses.

In the last case with an actual HPT stage upstream of the duct, the exit flow field is again dominated by the strut wakes (Fig. 6.4 A), the low momentum fluid at the outer boundary

layer (Fig. 6.4 B) and four vortices (Fig. 6.4 D) stemming from the HPT vane wakes, modulated by the HPT purge flow. Overall, the total pressure field at the exit plane comes close to a combination of the first two cases (clean inflow and case with IGVs). The strut wake (Fig. 6.4 A) width appears similar to the case with IGVs and is again wider as in the case with rotating bars. The low energy region in the wake extends from 30% channel height upwards, in between the two cases of clean inflow and with IGVs. A comparison of the tip end-wall losses (Fig. 6.4 B) show a similarity to the clean inflow case and indicate a slight shift to the rotor wake leeward side of the strut (similar to the case with IGVs). For the case with the HPT, the losses are again related to the boundary layer that may get superimposed by losses related to the mixing process of the tip leakage vortex and the purge air injected up- and downstream of the unshrouded HP blade.

TCF Throughflow

Figure 7 shows the oil flow visualization pictures for the hub end-wall in the five-hole-probe passage (in-between strut I and II) for all four cases in the view A.L.F.. The corresponding view at the casing is added for the three cases in the AnCa.

In all three AnCa results, the same viscosity of the oil was used, allowing for a direct comparison of the wall shear stress trajectories. For better understanding of the flow behaviour Figure 8 shows the static pressure coefficient along the hub and the casing in the middle of the passage.
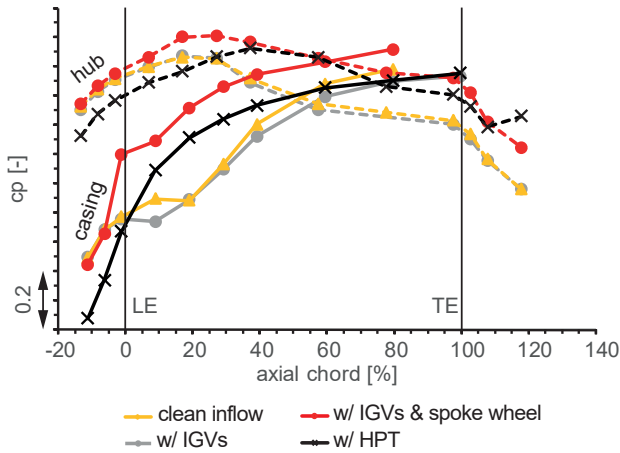
In the case with clean inflow (Fig. 7.1), the outer end-wall flow is comparable with the investigations done by Göttlich (2011) in a separated duct. A separation line can be detected at the 8% axial chord length, indicated by a red dashed line. The indication is based on a deflection of the flow in circumferential direction. In addition, Fig. 8 shows the start of a plateau at this position, an indication for a separation. Downstream of the separation line, a region of reversed flow can be traced. The reattachment lines (convergent sheer stress lines) marked in green can be found at 55% axial chord. This is the connection between two saddle points (Fig. 7.1 S2 and S3) close to the strut end-wall and the point where all the shear stress lines have their origin (Fig. 7.1 O). The periodicity in the passage is triggered by the two adjacent struts. This leads to the origin being exactly in the middle between the two displayed struts I and II. From this origin, one part of the flow is forming the back flow, while the other part flows downstream towards the LPT vanes. The reversed flow at mid-pitch is convected up to the separation line, forming another saddle point (Fig. 7.1 S1). Interesting to note is that in the reversed flow region, two beginning vortical structures in the shear stresses can be distinguished (foci (F1 and F2)). Close to the corner towards the strut end-wall another vortical structure can be detected, where its formation is highlighted in Fig. 9 and derived from a compressor cascade flow (Karakasis, et al., 2010). This vortex is pushed towards midspan and is marked in green in Fig. 9.

Further, derived from the oil flow, Fig. 9 illustrates the path of the horseshoe vortex from the lower strut leading edge and indicates the radial pressure gradient in yellow. Similar to the compressor cascade cross-passage flow (Karakasis, et al., 2010), the low momentum strut end-wall flow is driven by the
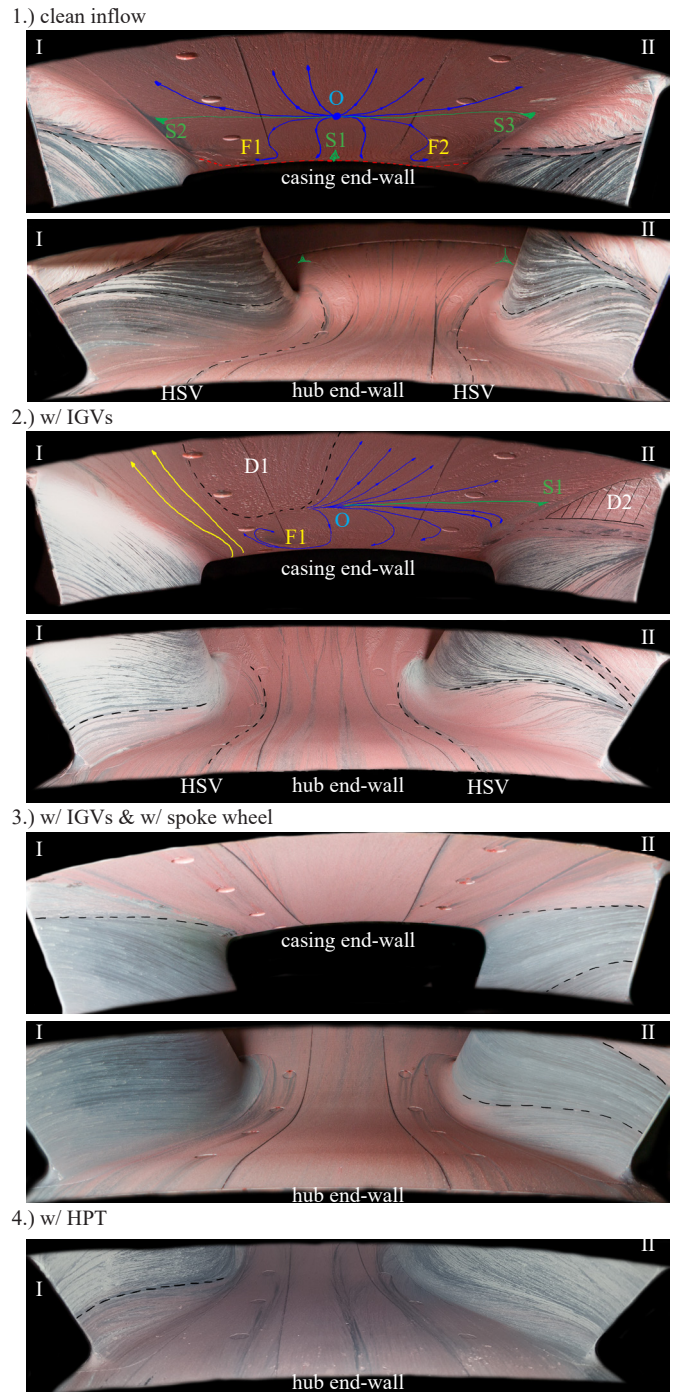
Figure 7: Flow Visualization of the four cases, casing and hub flow (view is A.L.F.)

radial pressure gradient and follows a smaller bending radius. This leads to a migration of the hub boundary layer up towards the strut boundary layer (further called cross-passage flow), visible as red oil traces in the flow visualisation (Fig. 7.1). In the absence of inlet swirl, this flow migration occurs symmetrically at both strut end-walls. When the radial pressure gradient reaches zero at 55% axial chord length (indicated by the similar pressure in the static pressure coefficient), the wall shear trajectories show a point of inflection. Downstream, the adverse radial pressure gradient causes the wall shear stress trajectories to change their

Figure 8: Static pressure distribution at the hub and casing end-walls

Legend: clean inflow — w/ IGVs & spoke wheel — w/ IGVs — w/ HPT

Figure 9: Symbolic duct flow for the case without IGVs

concavity. Further caused by the radial adverse pressure gradient a cross-passage flow from the tip can be observed. This cross-passage flow starts to roll up and forms a vortex that partially detaches from the strut end-wall. Its sense of rotation is indicated by red stripes on top of the white painting. Moreover, this vortical structure is responsible for the loss core in the duct exit flow (see Fig. 6.1 C).

For the case with IGVs, the inflow is pre-swirled with thin steady wakes entering the duct. Thus, the flow distribution throughout the duct is asymmetric showing wake related avenues in the duct hub end-wall (Fig. 7.2). In theory (Dominy & Kirkham, 1995), swirl in a non-strutted duct allows the flow to withstand stronger axial pressure gradients before separation. In the present case, though, the swirl was not imposed homogeneously all along the channel height, but in opposite direction at the hub and the casing. Therefore the additional swirl induced radial pressure gradient is not strong enough to suppress the separation and it extends only in a partial section of the channel. The separation line is visible at 0% axial chord length and in agreement with the pressure coefficient distribution of Fig. 8. Unfortunately, the duct outer curvature does not allow to mark the separation line in Fig. 7.2 anymore. The reattachment line moved 8% axial chord upstream, compared to the clean inflow case. The corresponding origin is not at mid-pitch anymore and the wall shear stress trajectories out of the origin are showing a movement towards the surface of strut II. A focus point (Fig. 7.2 F1) can be distinguished directly upstream of the origin, while downstream a zone with almost no wall shear stresses is marked in Fig. 7.2 as D1. The corresponding loss core at the exit plane (in Fig. 6.2) is insignificant compared to the loss core close to the strut leeward side (C).

Similar to the clean inflow case, the radial pressure gradient (after 57% axial chord length, the adverse radial pressure gradient) cause a cross passage flow at the strut end-wall. While the cross-passage flow from the hub again does not roll up, the cross-passage flow from the tip does. The rolled-up vortex appears to be strengthened by the casing swirl in the present case. A closer look at the upper corner of the strut leeward side indicates even a detached flow behaviour
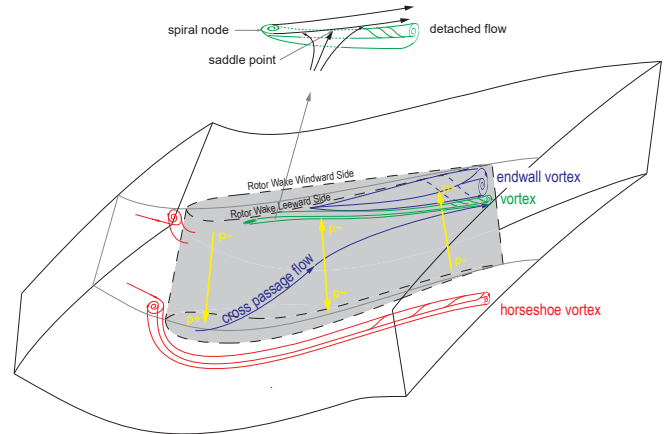
(Fig. 7.2 D2), not showing red projection lines of a helix anymore. The loss caused by the vortex core is visible in the TCF exit total pressure (Fig. 6.2 C). The corresponding URANS simulation shows qualitatively the enhancement of this core by the tip related horseshoe vortex (Fig. 10).

As already mentioned, the flow characteristics on the surface of strut I (visible in Fig. 7.2) are different due to the incoming swirl. Close to the strut end-wall, a non-separated casing flow is seen based on the wall shear stress trajectories (Fig. 7.2 yellow lines).

The hub end-wall flow shows structures emanating from the IGVs. These are formed by a vorticity distribution similar to the observations by Zerobin et al. (2017). To get an insight into the duct flow, Figure 11 presents the streamlines obtained from CFD in the duct passage, with the streamwise vorticity at the duct inlet and exit. This plot shows the duct in a forward looking aft perspective, where the vortical cores are indicated by their sense of rotation, either blue (counter - clockwise) or in red (clockwise). While the traces of the black streamlines represent periodic structures from the IGVs, the purple ones indicate the behaviour of the hub related horseshoe vortex. The simulation makes it clear, that the vortices from the IGVs are responsible for the roll-up of the streamlines. The vortical cores are still visible at the exit plane according to Fig. 11 and cause the low energy regions seen in the experimental results (Fig. 6.2 E). Moreover, both the IGV related structures and the hub-sided horseshoe vortex are also visible as lines of reduced oil paint in Fig. 7.2 (hub end-wall).

On the corresponding strut surface (I in Fig. 7.2), the radial fluid migration from the hub is visible, ending on the strut trailing edge at about 30% channel height. In the tip region, the boundary layer of the strut itself is visible, showing a zone of low wall shear stress, without any flow separation close to the trailing edge. Both windward side horseshoe vortices (at the hub and tip) stay away from the end-walls, as indicated in Fig. 10 and Fig. 11 (Strut left hand side).

In the case with the spoke wheel, the oil flow visualization gives results which are very different from the observations from the two cases described above (Fig. 7.3). Most importantly, the flow at the casing shows no indication for
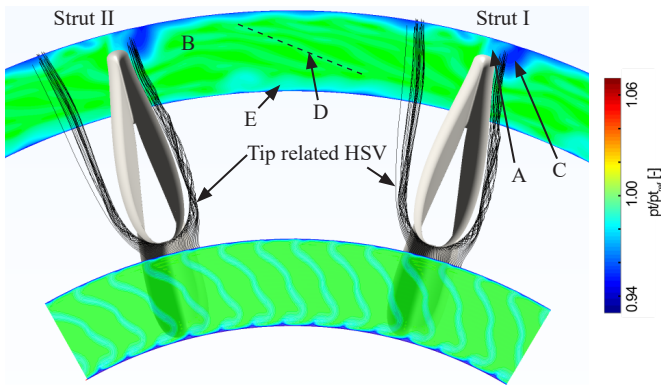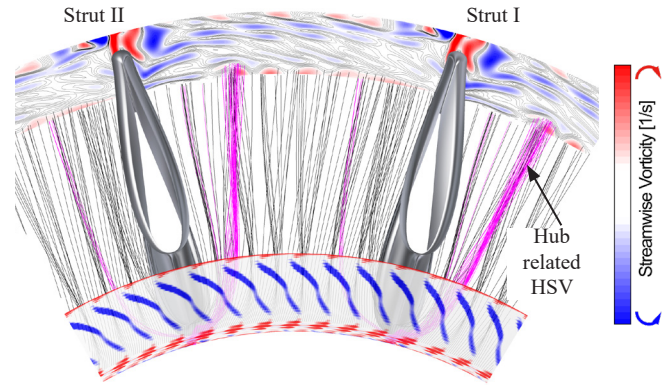
Figure 10: Tip streamlines, with total pressure contours at the duct inlet and exit for the case w/ IGVs (view is F.L.A)

Figure 11: Hub streamlines, with streamwise vorticity contours at the duct inlet and exit for the case w/ IGVs (view is F.L.A)

a separation anymore. The wall shear stress trajectories are visible along the whole axial chord, slightly bending towards the leeward side of the strut. The changes in the casing flow can be attributed to the strength of the tip flow. Compared to an HPT in the studies of Sanz et al. (2009), the spoke wheel does not produce a tip leakage vortex in the classic way. However, the tip jet and a pair of trailing vortices (or tip vortices) energise the boundary layer at the casing, suppressing the separation. Further the remaining thickness of the oil paint in the channel is significantly thinner, compared to the previously described cases. This implies higher wall shear stresses caused by a steeper velocity gradient close to the wall.

The oil flow at the hub again shows structures emanating from the IGVs, this time only visible up to 10% axial chord (Fig. 7.3). In addition, the lower horseshoe vortex can be seen throughout the channel, also staying away from the strut end-walls. Figure 8 indicates a strong increase in static pressure at the casing just before the strut leading edges. As soon as the flow enters the passage, the additional blockage of the strut changes the pressure rise gradient significantly, showing a small plateau in the static pressure distribution. Overall the radial pressure gradient at 10% axial chord is reduced and thus only a small amount of hub boundary layer fluid (red traces in Fig. 7.3) is migrating onto the strut surface. This migration ends at the strut trailing edge, at already 40% channel height. The cross-passage flow related to the casing continues to migrate onto the strut surface, but not as strongly as the hub boundary layer fluid. At this point, the cross-passage flow ends on both strut surfaces at about 85% channel height (Fig. 7.3).

For the case with the upstream HPT, accessibility constraints allowed visualization of the hub end-wall flow only (Fig. 7.4). A separation can be ruled out, due to the static pressure rise coefficient shown in Fig. 8. Additionally, the HPT - induced effects cause the pressure coefficient to start at a lower level. The radial pressure gradient itself is increased by 13% at the inlet compared to the case with the spoke wheel. The beginning of the adverse pressure gradient shifts further downstream and starts at 75% axial chord instead of at 60% for the case with spoke wheel. This might be the reason why no fluid migration from the outer end-wall onto the strut surface can be distinguished in the oil flow (Fig. 7.4). Anyway, since

the radial pressure gradient appears to be similar after 10% axial chord the cross-passage flow from the hub end-wall onto the strut surface can be identified and is comparable to the case with spoke wheel.

The hub flow visualisation in Fig. 7.4 shows structures emanating from the HPT stator wakes (similar to the before mentioned IGVs from Fig. 7.2). Since these wakes are much stronger than the IGV wakes, they do not mix out throughout the duct.

Total pressure loss comparison

Figure 12 presents the total pressure loss comparison for all four cases. As mentioned above, the Mach number for the case with the HPT was not perfectly matched to the three AnCa conditions. The clean inflow case shows lowest losses. With IGVs, the losses are increased by 8%, due to the wake mixing in the duct and the changes in the endwall flow. For the setup with IGVs, a Mach number variation was performed, and an approximately linear loss dependence on Mach number is observed. The addition of the spoke wheel leads to a 44% increase in loss, compared to the reference case. This increase is expected since additional losses from the rotating bar system enter and mix out through the duct. These additional losses reduce the overall pressure level in the core flow, visible in the contour plot of Fig. 6. When looking at the general flow behaviour in the duct, the separation is not present anymore
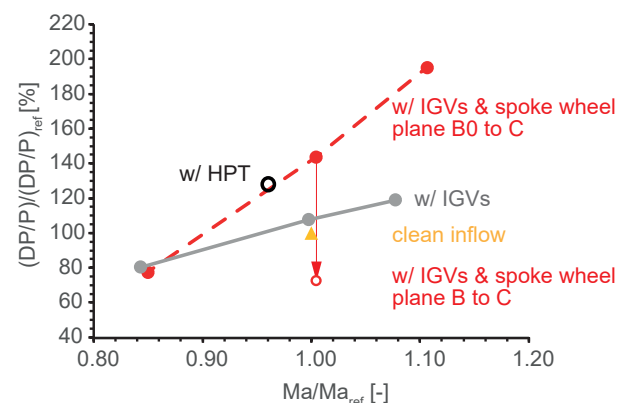
Figure 12: Total pressure loss comparison

and the radial fluid migration is reduced, compared to the case with IGVs. Furthermore, there is a reduction in low momentum fluid from the end-walls at the duct exit. These findings suggest that the additional losses caused by the spoke wheel are offset to the reduction of the end-wall losses. For this case, another Mach number sensitivity study of -15 and +10% was performed (red dashed line in Fig. 12). While keeping the reduced speed of the spoke wheel constant, the gradient of the losses changes in respect to the case with IGVs only. In addition, there is no significant difference in loss level at the low Mach number operating point.

Comparing the annular cascade case with the spoke wheel to the case with the actual HPT must be done with caution. Two different inlet planes (respectively, B0 for AnCa and B for HPT) are used to calculate the duct loss. The direct loss comparison is difficult since the wakes of the rods decay to a certain amount in-between these two planes and this mixing process needs to be addressed. In addition, there are differences in the rod diameter and HPT rotor blade trailing edge thickness due to mechanical constraints so the wakes of the rods may not be fully comparable to the HPT rotor wakes. Anyway to give an idea of the influence of the mixing process between plane B0 and B, the total pressure loss between planes B and C as well as between planes B0 and C were determined by means of the URANS simulation of the AnCa. The difference is subtracted from the loss measured with the five-hole probe, showing a 70 % reduction for the spoke wheel case (Fig. 12, shifted red circle w/ IGVs and spoke wheel plane B to C). Even though the new value of the duct loss depends on the URANS prediction of the wake mixing process, the extra losses induced by the HPT stage become visible. Namely, these would be the stronger wakes, secondary vortices, tip leakage flow, and pressure fluctuations, modulated by stator-rotor interaction.

CONCLUSIONS

The main conclusions of this study are that an engine-representative turbine center frame duct – with separation-free flow behind an HPT stage - can separate in clean inflow testing, when no rotating structures are present. For a designer, this observation highlights the danger of drawing conclusions from testing an TCF under clean inflow conditions. A TCF duct design may be too conservative if only clean inflow testing is used. In this case, the potential for duct length and weight reductions would not be fully realized.

This study underlines the challenges that may arise in comparing TCF duct pressure losses and demonstrates that clean inflow testing cannot provide a representative TCF duct loss level or relevant inlet conditions for the downstream LPT. Only conclusions regarding the radial exit profiles, drawn from the clean inflow test, match reasonably well to a case with an HPT stage upstream. At the same time, the findings of this investigation complement those of earlier studies showing a strong link between the flow separation and the rotor tip flow.

NOMENCLATURE

cp	pressure coefficient [-]
p	pressure [bar]
DP	differential pressure [bar]
Ma	Mach number [-]
T	temperature

Subscripts

s	static value
t	total value
ref	reference case – clean inflow

Abbreviations

ADP	Aero Design Point
A.L.F	Aft Looking Forward
AnCa	High Speed Annular Cascade
CFD	Computational Fluid Dynamics
FHP	Five-Hole Probe
F.L.A	Front Looking Aft
HP	High Pressure
HPT	High Pressure Turbine
HPV	High Pressure Vane
HSV	Horseshoe Vortex
IGV	Inlet Guide Vane
ITD	Intermediate Turbine Duct
TCF	Turbine Centre Frame
LP	Low Pressure
LE	Leading Edge
NACA	National Advisory Committee for Aeronautic
RANS	Reynolds Averaged Navier Stokes
TTTF	Transonic Turbine Test Facility
TE	Trailing Edge
URANS	Unsteady Reynolds Averaged Navier Stokes
SW	Spoke Wheel

REFERENCES

Bauinger S., Marn A., Göttlich E., and Heitmeier F. (2017). Influence of Pressure Fluctuations on the Mean Value of Different Pneumatic Probes. International Journal of Turbomachinery, Propulsion and Power 2 (13), DOI: 10.3390/ijtpp2030013

Dominy R. G. and Kirkham D. A. (1995). The influence of swirl on the performance of intermediate diffusors. VDI Berichte, Band 1186, pp. 107-129

Dominy R. G. and Kirkham D. A. (1996). The Influence of Blade Wakes on the Performance of Inter-Tubine Diffusors. Journal of Turbomachinery 118(2), pp. 347-352

Faustmann C. and Göttlich E. (2014). Aerodynamics and Acoustics of Turning Mid Turbine Frames in a Two Shaft Test Turbine. Proceedings of the ASME Turbo Expo, GT2014-25568

Göttlich E. (2011). Research on the aerodynamics of intermediate turbine diffusors. Progress in Aerospace Science 47(4), pp. 249-279

Göttlich E., Marn A., Pecnik R., Malzacher J.F., Schennach O. and Pirker H.P. (2007). The influence of blade tip gap variation on the flow through an aggressive S-shaped intermediate turbine duct - Part II. Proceedings of the ASME Turbo Expo, GT2007-28069

Karakasis M. K., Naylor E. M. J., Miller R. J. and Hodson H. P., (2010). The effect of an upstream compressor on a non-axisymmetric s-duct. Proceedings of ASME Turbo Expo, GT2010-23404

Marn A., Göttlich E., Pecnik R., Malzacher J.F., Schennach O. and Pirker H.P. (2007). The influence of blade tip gap variation on the flow through an aggressive S-shaped intermediate turbine duct - Part I. Proceedings of the ASME Turbo Expo, GT2007-27405

Mimic D., Drechsel B., Herbst F., (2017). Correlation between pressure recovery of high loaded annular diffusors and integral stage design parameters. Proceedings of ASME Turbo Expo, GT2017-63586

Sanz W., Collins M., Pecnik R., Marn A., and Göttlich E. (2009). Numerical Investigation of the Effect of Tip Leakage Flow on an Aggressive S-Shaped Intermediate Turbine Duct. Proceedings of the ASME Turbo Expo, GT2009-59535

Schulte V. and Hodson H. (1998). Unsteady Wake-Induced Boundary Layer Transition in High Lift LP Turbines, Journal of Turbomachinery 120(1), DOI 10.1115/1.2841384.

Steiner M., Zerobin S., Bauinger S., Heitmeir F., Göttlich E. (2017). Development and Commissioning of a Purge Flow System in a Two Spool Test Facility. 12th European Conference on Turbomachinery Fluid dynamics & Thermodynamics, ETC2017-115

Sumner D. (2013). Flow above the free end of a surface-mounted finite-height circular cylinder: A review. Journal of Fluids and Structures 43, pp. 41-63

Zerobin S., Peters A., Bauinger S., Ramesh A., Steiner M., Heitmeir F. and Göttlich E. (2017). The behavior of turbine center frames under the presence of purge flows. Proceedings of ASME Turbo Expo, GT2017-63606